Precision study of W^-W^+H production including parton shower effects at CERN Large Hadron Collider*

Huan-Yu Bi(毕环宇)[1,2] Ren-You Zhang(张仁友)[1,2;1)] Wen-Gan Ma(马文淦)[1,2] Yi Jiang(蒋一)[1,2]
Xiao-Zhou Li(李晓周)[1,2] Peng-Fei Duan(段鹏飞)[3]

[1]State Key Laboratory of Particle Detection and Electronics, University of Science and Technology of China, Hefei 230026, China
[2]Department of Modern Physics, University of Science and Technology of China, Hefei 230026, China
[3]City College, Kunming University of Science and Technology, Kunming 650051, China

Abstract: The precision study of W^-W^+H production with subsequent $W^\pm \to l^\pm\overset{(-)}{\nu}_l$ and $H \to b\bar{b}$ decays at the Large Hadron Collider (LHC) aids in the investigation of Higgs gauge couplings and the search for new physics beyond the standard model. In this study, we calculate the shower-matched next-to-leading order QCD and electroweak (EW) corrections from the $q\bar{q}$ annihilation and photon-induced channels to the W^-W^+H production at the 14 TeV LHC. We deal with the subsequent decays of Higgs and $W^\pm$ bosons by adopting the MADSPIN method. Both the integrated cross section and some kinematic distributions of $W^\pm$, H, and their decay products are provided. We find that the QCD correction significantly enhances the leading-order differential cross section, while the EW correction from the $q\bar{q}$ annihilation channel obviously suppresses it, especially in the high energy phase-space region, due to the Sudakov effect. The $q\gamma$- and $\gamma\gamma$-induced relative corrections are positive and insensitive to the transverse momenta of $W^\pm$, H, and their decay products. These photon-induced corrections compensate the negative $q\bar{q}$-initiated EW correction, and become the dominant EW contribution as the increment of the pp colliding energy. The parton shower (PS) effects on kinematic distributions are not negligible. The relative PS correction to the b-jet transverse momentum distribution can exceed 100% in the high $p_{T,b}$ region. Moreover, we investigate the scale and PDF uncertainties, and find that the theoretical error of the QCD + EW + $q\gamma$ + $\gamma\gamma$-corrected integrated cross section mainly originates from the renormalization scale dependence of the QCD correction.

Keywords: Higgs, gauge coupling, QCD+EW correction, parton shower

PACS: 12.15.Lk, 12.38.Bx, 14.70.Fm **DOI:** 10.1088/1674-1137/43/12/123103

1 Introduction

The Higgs mechanism is responsible for the electroweak (EW) symmetry breaking and the origin of masses of elementary particles [1–5]. Thus, it plays an important role in the standard model (SM). The Higgs boson was discovered in 2012 at the CERN Large Hadron Collider (LHC) [6, 7]. One of the main tasks presently at the LHC is to study the spin and CP properties of the Higgs boson, and the Higgs gauge and Yukawa interactions in detail. To understand the Higgs boson in the most accurate way, not only the main Higgs production channels, but also rare processes that can be sensitive to new physics, should be studied [8].

The precise phenomenological study of $VV'H$ (V, $V' = W$ or Z) productions is helpful for the study of Higgs gauge couplings, since it can be used to determine the ratio of WWH coupling to ZZH coupling [9] and study Higgs anomalous gauge couplings [8]. The EW corrections to the $VV'H$ production at the LHC are directly related to the triple and quartic gauge couplings, such as WWZ, $WW\gamma$, $WWZZ$, $WWZ\gamma$, $WW\gamma\gamma$, and $WWWW$ couplings. $pp \to VV'H + X$ processes also contain $HHVV'$ couplings. Since there are no constraints on

Received 30 July 2019, Published online 11 November 2019

* Supported in part by the National Natural Science Foundation of China (11775211 and 11535002), the Applied Basic Research Programs of Yunnan Provincial Science and Technology Department (2016FB008) and the CAS Center for Excellence in Particle Physics (CCEPP)

1) E-mail: zhangry@ustc.edu.cn

these Higgs quartic gauge couplings so far, detecting the Higgs production in association with two gauge bosons at the LHC and future high-energy hadron colliders (FCC-hh and SPPC) may help us constrain the bounds on the Higgs quartic gauge couplings (even though the backgrounds of these processes could be very large) [10].

Strictly speaking, the EW symmetry breaking is determined by the shape of the Higgs potential. However, Higgs triple gauge couplings are also related to the EW symmetry breaking: The gauge invariance of the Higgs kinetic term implies the existence of Higgs quartic gauge interactions. These Higgs quartic gauge interactions would induce Higgs triple gauge interactions as well as the masses of weak gauge bosons, once the EW symmetry is spontaneously broken. Since the $VV'H$ productions at the LHC are directly related to the Higgs triple gauge couplings, the precision study of $pp \to VV'H+X$ can help understand the EW symmetry breaking and search for new physics beyond the SM.

The close examination of Higgs properties requires accurate theoretical predictions and precise experimental measurements on both signals and backgrounds. At the LHC, the $W^-W^+b\bar{b}$ is an important final state. Many SM and BSM processes are measured in this final state, such as top pair production, Higgs pair production [11, 12] and vector-like quark pair production [13]. The production channel $pp \to W^-W^+H \to W^-W^+b\bar{b}$ could likewise serve as an irreducible background to these processes. The top pair production with subsequent decay $t \to Wb$ at the LHC has been widely investigated over the past twenty years, and the Higgs pair production and decays into $W^-W^+b\bar{b}$, $\gamma\gamma b\bar{b}$, and $\tau^-\tau^+b\bar{b}$ final states have been studied at the high-luminosity LHC [11]. The W^-W^+H production at the QCD next-to-leading order (NLO) including parton shower (PS) matching has been investigated in Refs. [14–16]. A further precision study of W^-W^+H production should involve the shower-matched NLO QCD (QCD+PS) correction, the $q\bar{q}$-, $q\gamma$- and $\gamma\gamma$-initiated EW corrections, and subsequent decays of $W^\pm$ and Higgs bosons.

In this work, we study in detail the W^-W^+H production with subsequent $W^\pm \to l^\pm\overset{(-)}{\nu}_l$ and $H \to b\bar{b}$ decays at the LHC, i.e., $pp \to W^-W^+H \to l^+l^-\nu_l\bar{\nu}_l b\bar{b}+X$ ($l = e$ or μ), including the QCD+PS correction and the EW corrections from the $q\bar{q}$ annihilation and photon-induced channels. The rest of this paper is organized as follows. In Sec. 2 we describe the analytical calculation strategy in detail. In Sec. 3 we present the numerical results of the integrated cross section and some kinematic distributions. We also discuss theoretical uncertainties from the factorization and renormalization scales and parton distribution functions (PDFs). Finally, a short summary is provided in Sec. 4.

2 Calculation strategy

In this study, the precision calculation for the $pp \to W^-W^+H+X$ process involves the following partonic channels: (1) quark-antiquark annihilation $q\bar{q} \to W^-W^+H+(g/\gamma)$, (2) real light-quark emission $qg/\gamma \to W^-W^+H+q$, (3) gluon-gluon fusion $gg \to W^-W^+H$, and (4) photon-photon fusion $\gamma\gamma \to W^-W^+H$, where q spans across all five light flavors of quarks. The $q\bar{q}$ annihilation subprocesses are calculated up to the QCD+EW NLO,

$$\sigma_{q\bar{q}} = \sigma^{\rm LO}_{q\bar{q}} + \Delta\sigma^{\rm QCD}_{q\bar{q}} + \Delta\sigma^{\rm EW}_{q\bar{q}}, \quad (1)$$

where $\sigma^{\rm LO}_{q\bar{q}}$, $\Delta\sigma^{\rm QCD}_{q\bar{q}}$ and $\Delta\sigma^{\rm EW}_{q\bar{q}}$ are the $O(\alpha^3)$, $O(\alpha^3\alpha_s)$, and $O(\alpha^4)$ contributions from the $q\bar{q}$ annihilation subprocesses, respectively. The subprocesses with qg and $q\gamma$ initial states are calculated only at the LO, and the corresponding cross sections are denoted as σ_{qg} and $\sigma_{q\gamma}$. The PDF counterterm corrections from the $q \to q+g$, $q \to q+\gamma$, $g \to q+\bar{q}$, and $\gamma \to q+\bar{q}$ parton splittings should be included in $\Delta\sigma^{\rm QCD}_{q\bar{q}}$, $\Delta\sigma^{\rm EW}_{q\bar{q}}$, σ_{qg}, and $\sigma_{q\gamma}$, respectively, for IR safety[1)]. Because of the large gluon density in the proton at high-energy hadron colliders, the loop-induced channel $gg \to W^-W^+H$ is taken into account in our precision QCD calculation, although the LO contribution of the gg fusion channel is one order of α_s higher than the NLO QCD correction from the $q\bar{q}$ annihilation channel. For the $\gamma\gamma$ fusion channel, the NLO EW correction is negligible, and we consider only its LO contribution to the $pp \to W^-W^+H+X$ process, because the density of photon in the proton is much lower than that of colored partons (i.e., gluon and light quarks). We generate all Feynman diagrams and amplitudes for these partonic channels by adopting the FEYNARTS package [17], and present some representative Feynman diagrams in Fig. 1. Then, the corrected cross section for the $pp \to W^-W^+H+X$ process without matching to the parton shower, calculated in this study, is given by

$$\sigma^{\rm QCD+EW+q\gamma+\gamma\gamma} = \sigma^{\rm LO} + \Delta\sigma^{\rm QCD} + \Delta\sigma^{\rm EW} + \sigma_{q\gamma} + \sigma_{\gamma\gamma}, \quad (2)$$

where the LO cross section, QCD correction, and EW correction are defined as[2)]

1) There are two types of PDF counterterm corrections from the $q \to q+\gamma$ splitting, which correspond to the P_{qq} and $P_{\gamma q}$ splitting functions, respectively. The EW PDF counterterm correction induced by the splitting function P_{qq} is absorbed into $\Delta\sigma^{\rm EW}_{q\bar{q}}$, while the correction induced by the splitting function $P_{\gamma q}$ as well as the PDF counterterm correction from the $\gamma \to q+\bar{q}$ splitting is absorbed into $\sigma_{q\gamma}$.

2) In this paper, we define $\Delta\sigma^{\rm EW}$ as the EW correction from the $q\bar{q}$ annihilation channel in order to show the photon-induced contributions ($\sigma_{q\gamma}$ and $\sigma_{\gamma\gamma}$) more clearly.

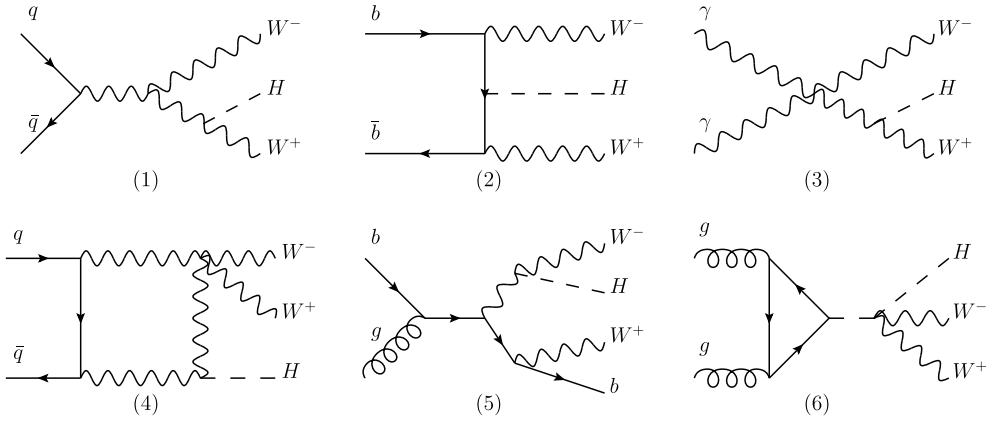

Fig. 1. Representative Feynman diagrams for partonic processes contributing to $pp \to W^-W^+H+X$ process.

$$\sigma^{\rm LO} = \sigma^{\rm LO}_{q\bar{q}},\ \Delta\sigma^{\rm QCD} = \Delta\sigma^{\rm QCD}_{q\bar{q}} + \sigma_{qg} + \sigma_{gg},\ \Delta\sigma^{\rm EW} = \Delta\sigma^{\rm EW}_{q\bar{q}}, \tag{3}$$

and $\sigma_{gg} \sim O(\alpha^3\alpha_s^2)$ and $\sigma_{\gamma\gamma} \sim O(\alpha^3)$ are the lowest order contributions of gg and $\gamma\gamma$ fusion channels, respectively. Since the calculation of the NLO QCD correction was presented in Refs. [14–16], we describe only the calculation of the EW correction in this section.

In the calculation of $\sigma^{\rm LO}$, $\Delta\sigma^{\rm QCD}$, $\Delta\sigma^{\rm EW}$ and $\sigma_{q\gamma}$, we adopt the G_μ scheme [18–20] (i.e., $\alpha = \alpha_{G_\mu}$) for all the EW couplings. This fine structure constant scheme is suitable for the EW correction due to the large EW Sudakov logarithms caused by the soft or collinear weak gauge-boson exchange at high energies [21, 22]. However, in the evaluation of the $\gamma\gamma$ fusion channel, we adopt the mixed scheme [23], where the fine structure constant is assumed as $\alpha = \alpha(0)$ and $\alpha = \alpha_{G_\mu}$ for electromagnetic and weak couplings, respectively. In the mixed scheme, the mass-singular terms $\ln(m_f^2/\mu^2)$ $(f = e,\mu,\tau,u,d,c,s,b)$ from the vacuum polarization at EW NLO can be either canceled between the external photons and the corresponding electromagnetic couplings, or be absorbed into α_{G_μ} in genuine weak couplings. Thus, the mixed scheme is more suitable for performing a high-order perturbative calculation for the processes with external photon legs[1)].

The ultraviolet (UV) and infrared (IR) divergences appeared in the NLO EW calculation are regularized in the dimensional regularization scheme. The complicated five-point loop integrals encountered in the virtual correction can be decomposed into four-point loop integrals by employing the Passarino-Veltman algorithm [24]. For four-point loop integrals, the numerical instability induced by small Gram determinant at some phase-space region can be solved by adopting the quadruple precision arithmetic, as in Refs. [20, 25]. The electric charge is renormalized in the G_μ scheme, and the relevant fields and masses are renormalized in the on-mass-shell renormalization scheme [26]. The real emission (i.e., the real photon emission and real light-quark emission) corrections are handled by adopting the two cutoff phase space slicing (TCPSS) method [27]. In the TCPSS method, two independent cutoff parameters, δ_s and δ_c, are introduced to decompose the final-state phase space into soft, hard-collinear, and hard-noncollinear regions, which are shown schematically in Fig. 7 of Ref. [27]. In this figure, the two triangles marked "m" should be included in the hard-collinear region. However, these two triangle regions are excluded, since a fixed upper limit of $1-\delta_s$ is used to calculate the hard-collinear contribution (cf. Eq.(2.35) of Ref. [27]). The two triangles marked "m" provide a vanishing contribution for $\delta_c \ll \delta_s$. In this work, we set $\delta_c = \delta_s/50$ according to the suggestion of Ref. [27]. We present the cutoff dependence of the NLO EW corrections to the W^-W^+H production from $u\bar{u}$ annihilation and $u(\bar{u})\gamma$ scattering at the LHC in Fig. 2 and Fig.3, re-

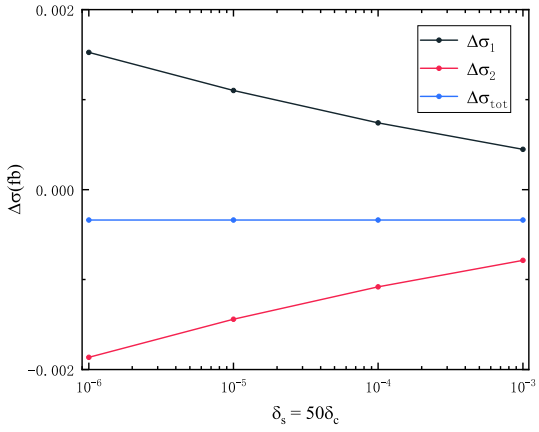

Fig. 2. (color online) δ_s dependence of NLO EW corrections to W^-W^+H production from $u\bar{u}$ annihilation at LHC. $\Delta\sigma_1$ and $\Delta\sigma_2$ represent the hard non-collinear correction and soft+collinear+virtual correction, respectively, and $\Delta\sigma_{\rm tot} = \Delta\sigma_1 + \Delta\sigma_2$.

1) Although the $\gamma\gamma$ fusion channel is calculated only at the LO because the NLO correction is negligible, we still suggest adopting the mixed scheme for this channel.

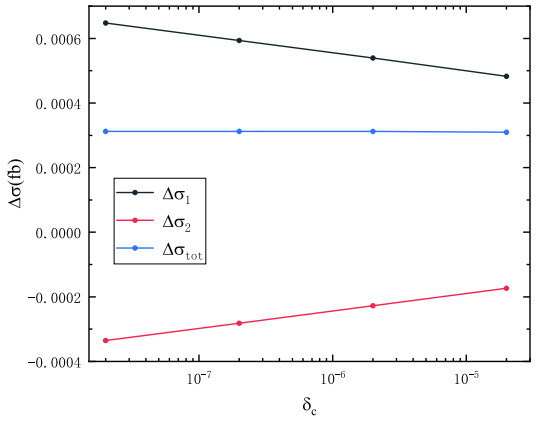

Fig. 3. (color online) δ_c dependence of NLO EW corrections to W^-W^+H production from $u(\bar{u})\gamma$ scattering at the LHC. $\Delta\sigma_1$ and $\Delta\sigma_2$ represent the non-collinear correction and collinear correction, respectively, and $\Delta\sigma_{\rm tot}=\Delta\sigma_1+\Delta\sigma_2$.

spectively. From the two figures, we may draw the conclusion that the total NLO EW corrections to the W^-W^+H production from different channels are all independent of the cutoff parameters within the calculation errors. As expected, the EW correction from the $q\bar{q}$ annihilation channel (i.e., the sum of the virtual correction and the real photon emission correction) and the $q\gamma$-induced correction (i.e., the real light-quark emission EW correction) are both UV and IR finite after absorbing the corresponding PDF counterterms.

Scalar and tensor integrals are calculated using our developed LOOPTOOLS package [28]. The PDFs are extracted by LHAPDF6 [29], and the phase-space integration is performed by employing the FORMCALC package [30]. The subsequent decays of $W^\pm$ and H are handled using the MADSPIN method [31]. The matching to the parton shower is implemented in the framework of MADGRAPH5+PYTHIA8+MADANALYSIS5+FASTJET [32–35]. To verify the correctness of our calculation, we recalculate the NLO QCD correction to W^-W^+H production with the same input parameters as in Refs. [14, 15], and find that our numerical results are in good agreement with the corresponding values in Refs. [14, 15] within calculation errors. Moreover, we calculate the NLO EW correction to ZZH production using our program and obtain $\delta_{\rm EW}\simeq 9\%$, which is consistent with that obtained using the newly developed MADGRAPH package [36].

A great number of W^-W^+H events originate from the W^-tH and $W^+\bar{t}H$ associated productions with subsequent top-quark decay $t\to Wb$, i.e., $pp\to bg/\gamma\to W^-tH\to W^-W^+Hb+X$, and $pp\to\bar{b}g/\gamma\to W^+\bar{t}H\to W^-W^+H\bar{b}+X$ (Fig. 1(5)). These events should be treated as the single top production, and thus should be subtracted carefully from our calculation to avoid double counting and to maintain the convergence of the perturbative description of the W^-W^+H production. In this study, we introduce four schemes to subtract the on-shell W^-tH and $W^+\bar{t}H$ events when handling the bg/γ- and $\bar{b}g/\gamma$-induced subprocesses. In scheme I, we assume that the event with a final b-jet can be rejected with 100% efficiency, such that the $pp\to bg/\gamma\to W^-W^+Hb+X$ and $pp\to\bar{b}g/\gamma\to W^-W^+H\bar{b}+X$ event samples can be easily excluded [15]. In scheme II, we adopt the diagram subtraction (DS) method [37, 38] to subtract the top-resonance effect. This subtraction scheme is defined as a replacement of the Breit-Wigner propagator

$$\frac{|M|^2(p_t^2)}{(p_t^2-m_t^2)^2+\Gamma_t^2m_t^2}\to\frac{|M|^2(p_t^2)}{(p_t^2-m_t^2)^2+\Gamma_t^2m_t^2}-\frac{|M|^2(m_t^2)}{(p_t^2-m_t^2)^2+\Gamma_t^2m_t^2}\Theta(\sqrt{\hat{s}}-M_W-m_t-M_H),\tag{4}$$

where p_t^2 is the squared momentum flowing through the intermediate top-quark propagator, and $\sqrt{\hat{s}}$ represents the parton-level colliding energy. In this scheme, the contributions from squared amplitudes with on-shell top quark are removed point by point over the entire phase space, and the gauge invariance is guaranteed in the limit $\Gamma_t\to 0$. In scheme III, we adopt the diagram removal (DR) method [39,40], i.e., we remove all the top-resonance diagrams at the amplitude level to subtract the top-resonance effect. This DR method violates gauge invariance. However, the authors of Refs. [39, 40] investigated the gauge dependence for the Wt and squark-pair productions in detail and found that the influence of gauge dependence in the DR scheme can be safely neglected in numerical studies. In scheme IV, we introduce the following subtraction term to remove the contributions from W^-tH and $W^+\bar{t}H$ productions with the subsequent top-quark decay at the cross-section level[1] [41],

$$\sigma_{\rm sub}=-[\sigma^{\rm LO}(pp\to bg/\gamma\to W^-tH+X)+\sigma^{\rm LO}(pp\to\bar{b}g/\gamma\to W^+\bar{t}H+X)]\times{\rm Br}(t\to Wb).\tag{5}$$

This scheme can maintain gauge invariance, since there is no diagram removal at the amplitude level. In Refs. [39, 42] the authors suggest imposing an invariant mass cut on W^+b and $W^-\bar{b}$ systems, which can be written in the form

$$|M_{Wb}-m_t|>\kappa\Gamma_t,\tag{6}$$

to exclude the W^-tH and $W^+\bar{t}H$ events, respectively. However, we do not adopt this scheme in our calculation, because the $pp\to bg/\gamma\to W^-W^+Hb+X$ and $pp\to\bar{b}g/\gamma\to W^-W^+H\bar{b}+X$ subprocesses cannot be properly handled using the TCPSS method after applying the invariant

1) We assume ${\rm Br}(t\to Wb)=100\%$ for simplicity.

mass cut in Eq. (6).

3 Numerical results

3.1 Input parameters

The Fermi constant and mass parameters are taken from the recent CERN yellow report "Handbook of LHC Higgs cross-sections: 4. Deciphering the nature of the Higgs sector" [43]:

$$M_W = 80.385\ \text{GeV},\ M_Z = 91.1876\ \text{GeV},\ m_t = 172.5\ \text{GeV},$$
$$M_H = 125\ \text{GeV},\ G_\mu = 1.1663787\times10^{-5}\ \text{GeV}^{-2}. \tag{7}$$

The top-quark decay width $\Gamma_t = 1.41$ GeV and the fine structure constant in the $\alpha(0)$ scheme $\alpha(0) = 1/137.035999139$ are taken from Ref. [44]. In the G_μ scheme, we obtain

$$\alpha = \alpha_{G_\mu} = \frac{\sqrt{2}}{\pi}G_\mu M_W^2\left(1-\frac{M_W^2}{M_Z^2}\right). \tag{8}$$

The strong coupling constant α_s is taken from the PDFs. The factorization and renormalization scales are set to be equal, i.e., $\mu_f = \mu_r = \mu$, and the central scale is chosen as $\mu_0 = M_T/2$ unless stated otherwise, where M_T is the sum of the transverse masses of final particles. We adopt the LUXqed_plus_PDF4LHC15_nnlo_100 PDFs [45] throughout the LO and NLO calculations, as in Refs. [46, 47]. All leptons and quarks except the top quark are treated as massless particles[1)], and the Cabibbo-Kobayashi-Maskawa (CKM) matrix is set to $\mathbf{1}_{3\times3}$. The W-boson decay branching ratio $\text{Br}(W^\pm \to l^\pm\overset{(-)}{\nu}_l) = 22.2\%$ is obtained using the MADSPIN program, and the Higgs-boson decay branching ratio $\text{Br}(H\to b\bar{b}) = 57.5\%$ is taken from Ref. [48].

3.2 Integrated cross sections

In Table 1, we present the LO and QCD + EW + $q\gamma + \gamma\gamma$ corrected integrated cross sections and the QCD, EW, $q\gamma$-induced, and $\gamma\gamma$-induced corrections ($\Delta\sigma^{\text{QCD}}$, $\Delta\sigma^{\text{EW}}$, $\sigma_{q\gamma}$, and $\sigma_{\gamma\gamma}$) for the W^-W^+H production at the 14 TeV LHC by employing the four different subtraction schemes mentioned above. The corresponding relative corrections are defined as

$$\delta_{\text{QCD}} = \frac{\Delta\sigma^{\text{QCD}}}{\sigma^{\text{LO}}},\ \delta_{\text{EW}} = \frac{\Delta\sigma^{\text{EW}}}{\sigma^{\text{LO}}},\ \delta_{q\gamma} = \frac{\sigma_{q\gamma}}{\sigma^{\text{LO}}},\ \delta_{\gamma\gamma} = \frac{\sigma_{\gamma\gamma}}{\sigma^{\text{LO}}}. \tag{9}$$

As expected, σ^{LO}, $\Delta\sigma^{\text{EW}}$, and $\sigma_{\gamma\gamma}$ are independent of the subtraction scheme, because the subtraction of the W^-tH and $W^+\bar{t}H$ events reduces only the contributions of the bg/γ and $\bar{b}g/\gamma$ scattering channels, respectively. The $q\gamma$-induced correction, which is insensitive to the subtraction scheme, is significant ($\Delta\sigma_{q\gamma} \simeq 0.59$ fb, $\delta_{q\gamma} \simeq 6.1\%$), and compensates the negative EW correction from the $q\bar{q}$ annihilation channel ($\Delta\sigma^{\text{EW}} = -0.58$ fb, $\delta_{\text{EW}} = -6.0\%$). The contribution from the $\gamma\gamma$ fusion channel is sizable ($\sigma_{\gamma\gamma} = 0.28$ fb, $\delta_{\gamma\gamma} = 2.9\%$), and thus should be taken into account in the precision EW calculation, especially when $\delta_{\text{EW}} + \delta_{q\gamma} \sim 0$. Subsequently, the full EW relative correction, defined as $\delta_{\text{EW}}^{(\text{full})} = \delta_{\text{EW}} + \delta_{q\gamma} + \delta_{\gamma\gamma}$, is obtained as $\delta_{\text{EW}}^{(\text{full})} = 2.7\%$ by adopting scheme I. The QCD corrections in scheme I, II, and III are almost the same ($\delta_{\text{QCD}} = 30\% \sim 31\%$), while the QCD correction in scheme IV is obviously overestimated, as we adopt the narrow-width approximation to subtract W^-tH and $W^+\bar{t}H$ events in scheme IV (see Eq.(5)). Since the difference between scheme I, II, and III are miniscule, and the b-jet veto can be easily implemented, we adopt only scheme I to deal with the $pp \to bg/\gamma \to W^-W^+Hb + X$ and $pp \to \bar{b}g/\gamma \to W^-W^+H\bar{b} + X$ subprocesses in the following discussion.

Table 1. LO and QCD + EW + $q\gamma + \gamma\gamma$ corrected integrated cross sections (in fb) for W^-W^+H production at the 14 TeV LHC for subtraction scheme I, II, III, and IV.

subtraction scheme	σ^{LO}	$\Delta\sigma^{\text{EW}}$	$\sigma_{\gamma\gamma}$	$\sigma_{q\gamma}$	$\Delta\sigma^{\text{QCD}}$	$\sigma^{\text{QCD+EW}+q\gamma+\gamma\gamma}$
I	9.65	−0.58	0.28	0.56	2.99	12.90
II				0.59	2.94	12.88
III				0.59	2.95	12.89
IV				0.59	3.83	13.77

The factorization/renormalization scale dependence of the LO and QCD + EW + $q\gamma + \gamma\gamma$ corrected integrated cross sections and the corresponding QCD, EW, $q\gamma$-induced and $\gamma\gamma$-induced corrections for the W^-W^+H production at the 14 TeV LHC are shown in Table 2. To estimate the theoretical error from the factorization/renormalization scale, we define the scale uncertainty at a given scale μ_0 as[2)]

$$\varepsilon_{\text{scale}}(\mu_0) = \frac{1}{\sigma(\mu_0)}\max\left\{\sigma(\mu)-\sigma(\mu')\,\middle|\,\mu,\mu'\in[\mu_0/2, 2\mu_0]\right\}. \tag{10}$$

We adopt two typical central scales for comparison: (1) $\mu_0^{(1)} = M_T/2$ and (2) $\mu_0^{(2)} = M_F/2$ ($M_F = 2M_W + M_H$), which are dependent and independent of the final-state phase space, respectively. The scale uncertainties at these two scales are denoted as $\varepsilon_{\text{scale}}^{(1)}$ and $\varepsilon_{\text{scale}}^{(2)}$. From Table 2, we can see that whatever the applied central scale, the scale uncertainties of σ^{LO}, $\Delta\sigma^{\text{EW}}$, $\sigma_{q\gamma}$ and $\sigma_{\gamma\gamma}$ are only about $0.4\% \sim 0.6\%$, while the scale uncertainties of $\Delta\sigma^{\text{QCD}}$ and $\sigma^{\text{QCD+EW}+q\gamma+\gamma\gamma}$ are much more significant and exceed 4%.

1) In this paper, the bottom-quark mass is set to zero in the calculation of the $pp \to W^-W^+H + X$ production process, but is kept to be nonzero when considering its subsequent Higgs-boson decay $H \to b\bar{b}$.

2) The scale uncertainties of $\Delta\sigma^{\text{QCD}}$, $\Delta\sigma^{\text{EW}}$, $\sigma_{q\gamma}$ and $\sigma_{\gamma\gamma}$ listed in Table 2 are normalized by $\sigma^{\text{QCD+EW}+q\gamma+\gamma\gamma}$, since $\Delta\sigma^{\text{QCD}}$, $\Delta\sigma^{\text{EW}}$, $\sigma_{q\gamma}$ and $\sigma_{\gamma\gamma}$ are regarded as the correction components of the corrected cross section $\sigma^{\text{QCD+EW}+q\gamma+\gamma\gamma}$.

Table 2. Scale dependence of LO and QCD + EW + $q\gamma + \gamma\gamma$ corrected integrated cross sections for W^-W^+H production at 14 TeV LHC.

	cross section /fb			$\varepsilon^{(1)}_{\rm scale}$ (%)	cross section /fb			$\varepsilon^{(2)}_{\rm scale}$ (%)
	$\mu_0^{(1)}/2$	$\mu_0^{(1)}$	$2\mu_0^{(1)}$		$\mu_0^{(2)}/2$	$\mu_0^{(2)}$	$2\mu_0^{(2)}$	
$\sigma^{\rm LO}$	9.61	9.65	9.63	0.41	9.65	9.71	9.71	0.62
$\Delta\sigma^{\rm QCD}$	3.36	2.99	2.75	4.73	3.39	3.04	2.74	5.00
$\Delta\sigma^{\rm EW}$	−0.60	−0.58	−0.55	0.39	−0.63	−0.60	−0.58	0.38
$\sigma_{q\gamma}$	0.59	0.56	0.53	0.47	0.61	0.58	0.55	0.46
$\sigma_{\gamma\gamma}$	0.25	0.28	0.31	0.47	0.23	0.26	0.29	0.46
$\sigma^{\rm QCD+EW+q\gamma+\gamma\gamma}$	13.21	12.90	12.67	4.19	13.25	12.99	12.71	4.16

This implies that the theoretical error induced by the renormalization scale is roughly one order of magnitude larger than that induced by the factorization scale. We may conclude that the scale uncertainty of the QCD + EW + $q\gamma + \gamma\gamma$ corrected cross section mainly originates from the renormalization scale dependence of the QCD correction, and the scale uncertainty of the LO cross section is underestimated, since the LO cross section does not depend on the strong coupling. The table also shows that the difference between the corrected cross sections at the dynamical scale $\mu_0^{(1)}$ and the fixed scale $\mu_0^{(2)}$ is very small (~0.7%). The EW correction from the $q\bar{q}$ annihilation channel is almost compensated by the $q\gamma$-induced correction, and thus $\delta_{\rm EW}^{\rm (full)} \approx \delta_{\gamma\gamma}$, at the 14 TeV LHC.

The QCD + EW + $q\gamma + \gamma\gamma$ corrected integrated cross section for $pp \to W^-W^+H + X$ at the 14 TeV LHC as a function of μ_r and μ_f, where μ_r and μ_f are two independent variables varying in the range of $\mu_r, \mu_f \in [\mu_0^{(1)}/2, 2\mu_0^{(1)}]$, is depicted in Fig. 4. From this contour plot, we can draw the following conclusions: (1) The QCD + EW + $q\gamma + \gamma\gamma$ corrected integrated cross section increases with the increment of μ_f, while it decreases with the increment of μ_r. (2) The μ_r dependence is much larger than the μ_f dependence. For example,

$$\begin{aligned}
&\sigma^{\rm QCD+EW+q\gamma+\gamma\gamma}\left(x_r = 1,\ x_f = 2\right) - \sigma^{\rm QCD+EW+q\gamma+\gamma\gamma}\left(x_r = 1,\ x_f = 0.5\right) = 0.07\ {\rm fb},\\
&\sigma^{\rm QCD+EW+q\gamma+\gamma\gamma}\left(x_r = 2,\ x_f = 1\right) - \sigma^{\rm QCD+EW+q\gamma+\gamma\gamma}\left(x_r = 0.5,\ x_f = 1\right) = -0.61\ {\rm fb},
\end{aligned} \tag{11}$$

where $x_r \equiv \mu_r/\mu_0^{(1)}$ and $x_f \equiv \mu_f/\mu_0^{(1)}$. These two conclusions are coincident with those obtained from Table 2.

As the factorization scale increases from $M_T/4$ to $4M_T$, the LO cross section of the $u\bar{u}$ channel increases gently at first and then decreases, the LO cross section of $d\bar{d}$ channel decreases, while the LO cross sections of $c\bar{c}$, $s\bar{s}$, and $b\bar{b}$ channels increase. Hence, the impact of the factorization scale on the total cross section is suppressed since all channels are summed. However, there is no cancelation between these channels when considering the renormalization scale dependence. Moreover, the renormalization scale uncertainty is underestimated at the LO, because the W^-W^+H production at the LO is a pure EW process. The renormalization scale uncertainty at the NLO is much larger than that at the LO. In conclusion, we may expect that the factorization scale dependence is weak compared to the renormalization scale dependence.

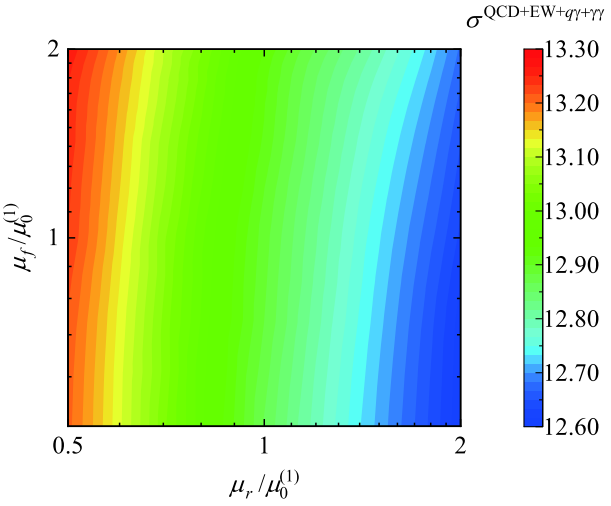

Fig. 4. (color online) QCD + EW + $q\gamma + \gamma\gamma$-corrected integrated cross section for $pp \to W^-W^+H + X$ at the 14 TeV LHC as a function of μ_r and μ_f.

The LO, QCD + EW + $q\gamma + \gamma\gamma$ corrected integrated cross sections and the corresponding QCD, EW, $q\gamma$-induced, and $\gamma\gamma$-induced (relative) corrections for the W^-W^+H production at the 13, 14 TeV LHC and a 33 TeV proton-proton collider are provided in Table 3. The QCD and photon-induced corrections (i.e., $\Delta\sigma^{\rm QCD}$, $\sigma_{q\gamma}$, and $\sigma_{\gamma\gamma}$) are positive and increase as the increment of the pp colliding energy, while the EW correction from the $q\bar{q}$ annihilation channel is negative and decreases as the increment of the colliding energy. The QCD correction is significant, and the relative correction can reach about 37%

Table 3. LO, QCD + EW + $q\gamma$ + $\gamma\gamma$ corrected integrated cross sections, and corresponding (relative) corrections for W^-W^+H production at 13TeV, 14 TeV LHC and a 33 TeV pp collider.

$\sqrt{S}$ /TeV	cross section /fb					
	$\sigma^{\rm LO}$	$\Delta\sigma^{\rm QCD}$	$\Delta\sigma^{\rm EW}$	$\sigma_{q\gamma}$	$\sigma_{\gamma\gamma}$	$\sigma^{\rm QCD+EW+q\gamma+\gamma\gamma}$
13	8.56	2.60	−0.51	0.47	0.23	11.35
14	9.65	2.99	−0.58	0.56	0.28	12.90
33	33.87	12.66	−2.27	3.93	1.56	49.75
$\sqrt{S}$ /TeV	relative correction (%)					
	$\delta_{\rm QCD}$	$\delta_{\rm EW}$	$\delta_{q\gamma}$	$\delta_{\gamma\gamma}$		
13	30.4	−6.0	5.5	2.7		
14	31.0	−6.0	5.8	2.9		
33	37.4	−6.7	11.6	4.6		

at a 33 TeV proton-proton collider. For the EW correction, the $q\gamma$-induced and $\gamma\gamma$-induced relative corrections increase quickly from 5.5% to 11.6% and from 2.7% to 4.6%, respectively, while the EW relative correction from the $q\bar{q}$ annihilation channel holds steady at $-6\% \sim -7\%$, as the pp colliding energy increases from 13TeV to 33 TeV. The ratio of the full EW correction to the QCD correction, $\delta_{\rm EW}^{\rm (full)}/\delta_{\rm QCD}$, is about 9% at the 14 TeV LHC and can exceed 25% at a 33 TeV proton-proton collider. Hence, the photon-induced correction would be the dominant EW contribution, and the full EW correction becomes increasingly important with the increment of the pp colliding energy.

PDF is another source of theoretical error for the scattering processes at hadron colliders. In this study, we adopt the LUXqed_plus_PDF4LHC15_nnlo_100 PDFs, which contains $N = 108$ PDF sets. The PDF uncertainties of the LO and QCD + EW + $q\gamma$ + $\gamma\gamma$ corrected integrated cross sections are given by [20,49]

$$\varepsilon_{\rm PDF}^{\rm X} = \frac{1}{\sigma^{\rm X}}\left[\sum_{i=1}^{N-1}(\sigma_i^{\rm X}-\sigma_0^{\rm X})^2\right]^{1/2}, \tag{12}$$

where $\mathrm{X} \in \{\mathrm{LO}, \mathrm{QCD}+\mathrm{EW}+q\gamma+\gamma\gamma\}$, and $\sigma_i^{\rm X}$ $(i = 0, \cdots, N-1)$ are the corresponding cross sections calculated using the i-th LUXqed_plus_PDF4LHC15_nnlo_100 PDF set. Thus, we obtain

$$\varepsilon_{\rm PDF}^{\rm LO} = 1.9\%, \quad \varepsilon_{\rm PDF}^{\rm QCD+EW+q\gamma+\gamma\gamma} = 1.7\%. \tag{13}$$

This clearly shows that the PDF uncertainty of the QCD + EW + $q\gamma$ + $\gamma\gamma$ corrected cross section is almost the same as the PDF uncertainty of the LO cross section, and thus the PDF uncertainties from the QCD, EW, $q\gamma$-induced, and $\gamma\gamma$-induced corrections are negligible. We also employ the NNPDF23_nlo_as_0119_qed PDFs in the initial-state parton convolution for comparison and find that the PDF uncertainties obtained using the LUXqed PDFs are much lower than the ones corresponding to the NNPDF23 PDFs. The small photon PDF uncertainty of the LUXqed PDFs was also discussed in Refs. [45, 47]. Compared to the scale uncertainty, the PDF uncertainty of the integrated cross section is much smaller, especially at the QCD+EW NLO. Thus, we do not consider the PDF uncertainty in estimating the theoretical error for the W^-W^+H production at the LHC.

3.3 Kinematic distributions

In this subsection, we present the LO and QCD + PS + EW + $q\gamma$ + $\gamma\gamma$-corrected kinematic distributions of final $W^\pm$ and Higgs bosons and their decay products for the W^-W^+H production at the 14 TeV LHC.

3.3.1 Distributions for $pp \to W^-W^+H + X$

The LO and QCD + PS + EW + $q\gamma$ + $\gamma\gamma$ corrected invariant mass distributions of the W-boson pair are plotted in the left panel of Fig. 5. The corresponding relative corrections induced by the electroweak and strong interactions ($\delta_{\rm EW}$, $\delta_{q\gamma}$, $\delta_{\gamma\gamma}$ and $\delta_{\rm QCD}$, $\delta_{\rm QCD+PS}$, $\delta_{\rm PS}$) are provided in the top-right and bottom-right panels, respectively[1)]. Both the LO and QCD + PS + EW + $q\gamma$ + $\gamma\gamma$ corrected invariant mass distributions of the W-boson pair reach their maxima in the vicinity of $M_{W^-W^+} \sim 200$ GeV and subsequently decrease approximately logarithmically with the increment of $M_{W^-W^+}$. The QCD+PS correction significantly enhances the LO W-boson pair invariant mass distribution in the entire plotted $M_{W^-W^+}$ region. The corresponding QCD relative correction gradually increases from 30% to approximately 40% as the increment of $M_{W^-W^+}$, while the QCD+PS relative correction holds steady at about 30%. For the EW correction, the contribution from the $q\bar{q}$ annihilation channel suppresses the LO W-boson pair invariant mass distribution, and the relative correction $\delta_{\rm EW}$ decreases from 0% to −20%, while the $q\gamma$-induced and $\gamma\gamma$-induced contributions enhance the LO W-

1) The PS relative correction is given by $\delta_{\rm PS} = \delta_{\rm QCD+PS} - \delta_{\rm QCD}$.

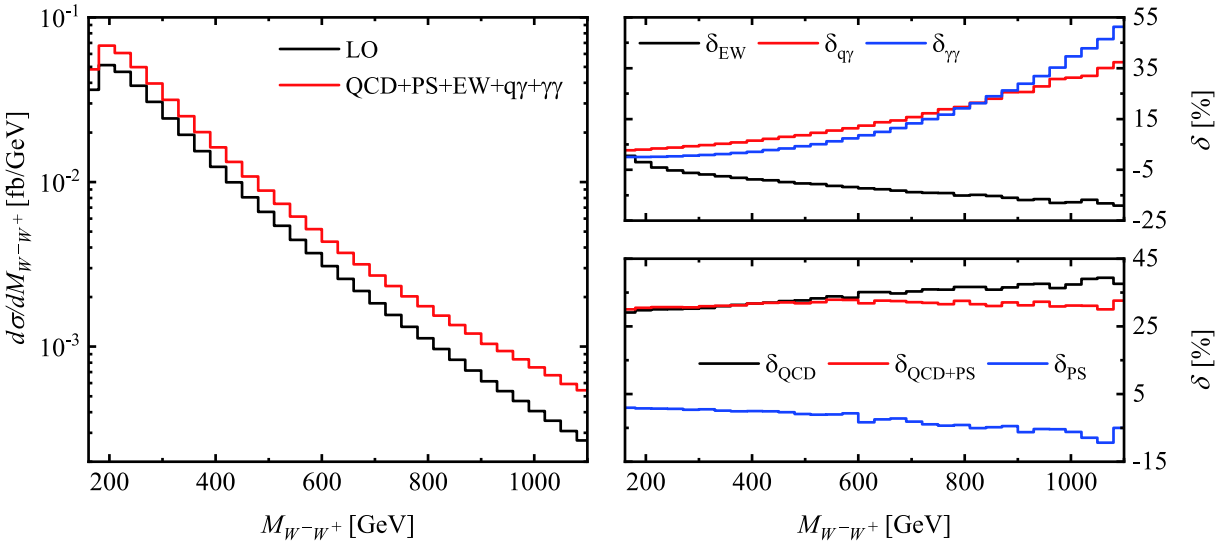

Fig. 5. (color online) W-boson pair invariant mass distributions and corresponding relative corrections for $pp \to W^-W^+H+X$ at the 14 TeV LHC.

boson pair invariant mass distribution, and the corresponding relative corrections $\delta_{q\gamma}$ and $\delta_{\gamma\gamma}$ increase rapidly from 3% to approximately 35% and from 0% to about 50%, respectively, as $M_{W^-W^+}$ increases from $2M_W$ to 1.1 TeV. This clearly shows that the full photon-induced correction, given by $\sigma_{\gamma-\text{induced}} = \sigma_{q\gamma} + \sigma_{\gamma\gamma}$, is larger than the QCD+PS correction in the high $M_{W^-W^+}$ region. Thus, the LO W-boson pair invariant mass distribution is mainly enhanced by the QCD+PS correction in the low $M_{W^-W^+}$ region, while it is mainly enhanced by photon-induced corrections in the high $M_{W^-W^+}$ region. The extremely large $\gamma\gamma$-induced correction at high invariant mass can also been seen in the invariant mass distribution of the W^-W^+Z system for $pp \to W^-W^+Z+X$ at the LHC [18][1)]. The considerable negative EW correction from the $q\bar{q}$ annihilation channel in the high $M_{W^-W^+}$ region is due to the well-known Sudakov double logarithms arising from the exchange of a virtual massive gauge boson in the loops [18, 20]. This large Sudakov virtual correction is obviously compensated by the positive photon-induced corrections ($\sigma_{q\gamma}$ and $\sigma_{\gamma\gamma}$), and the full EW correction enhances the LO W-boson pair invariant mass distribution. Therefore, the photon-induced channels should be considered for precision predictions at high energy colliders, especially in the high energy phase-space region.

The LO and QCD + PS + EW + $q\gamma + \gamma\gamma$ corrected transverse momentum distributions of the W^--boson and the corresponding relative corrections are presented in Fig. 6. Both the LO and QCD + PS + EW + $q\gamma + \gamma\gamma$ corrected distributions reach their peaks at $p_{T,W^-} \sim 45$ GeV and then decrease consistently as the increment of p_{T,W^-}. The QCD and QCD+PS relative corrections range from 30% to 40% and from 25% to 45%, respectively, as $p_{T,W^-} \in [0, 400]$ GeV. As p_{T,W^-} increases from 0 GeV to 400 GeV, the EW relative correction from the $q\bar{q}$ annihilation channel decreases from about −3% to −20%, while the relative corrections from the $q\gamma$ and $\gamma\gamma$ scattering channels are steady at about 5% and 1~4%, respectively. The total production cross section is dominated by the contribution from the low p_{T,W^-} region. In the vicinity of $p_{T,W^-} \sim 150$ GeV, the EW correction from the $q\bar{q}$ annihilation channel is almost compensated by the photon-induced corrections.

The LO and QCD + PS + EW + $q\gamma + \gamma\gamma$ corrected rapidity distributions of W^- and W^+ are depicted in the left panels of Figs. 7(a) and 7(b), respectively. The corresponding relative corrections are shown in the right panels. Both the LO and QCD + PS + EW + $q\gamma + \gamma\gamma$ corrected rapidity distributions of W^- are slightly larger than the ones corresponding to W^+ in the central rapidity region, however a little less than those of W^+ in the forward-backward rapidity region. The QCD correction significantly enhances the LO W-boson rapidity distributions, and the QCD+PS relative correction decreases from approximately 35% to 25% for both W^- and W^+ rapidity distributions as $|y_W|$ increases from 0 to 3. The EW relative correction from the $q\bar{q}$ annihilation channel is negat-

1) We calculate the cross sections for the $\gamma\gamma \to W^-W^+H$ and $u\bar{u} \to W^-W^+H$ channels, separately. The partonic cross section for the $\gamma\gamma$ fusion channel increases, while the cross section for the $u\bar{u}$ annihilation channel decreases, as the increment of the partonic colliding energy. We also investigate the photon and u-quark PDFs. We find that both PDFs decrease with the increment of Bjorken x, and the photon PDF decreases even faster than u-quark PDF. Thus, the enhancement of the effects of the photon-induced contributions in the high invariant mass region mainly due to the behaviour of partonic cross section. As for other kinematic distributions such as p_T distributions, since p_T is different from invariant mass and it is not directly related to the partonic colliding energy, the enhancement in the high p_T region is not obvious.

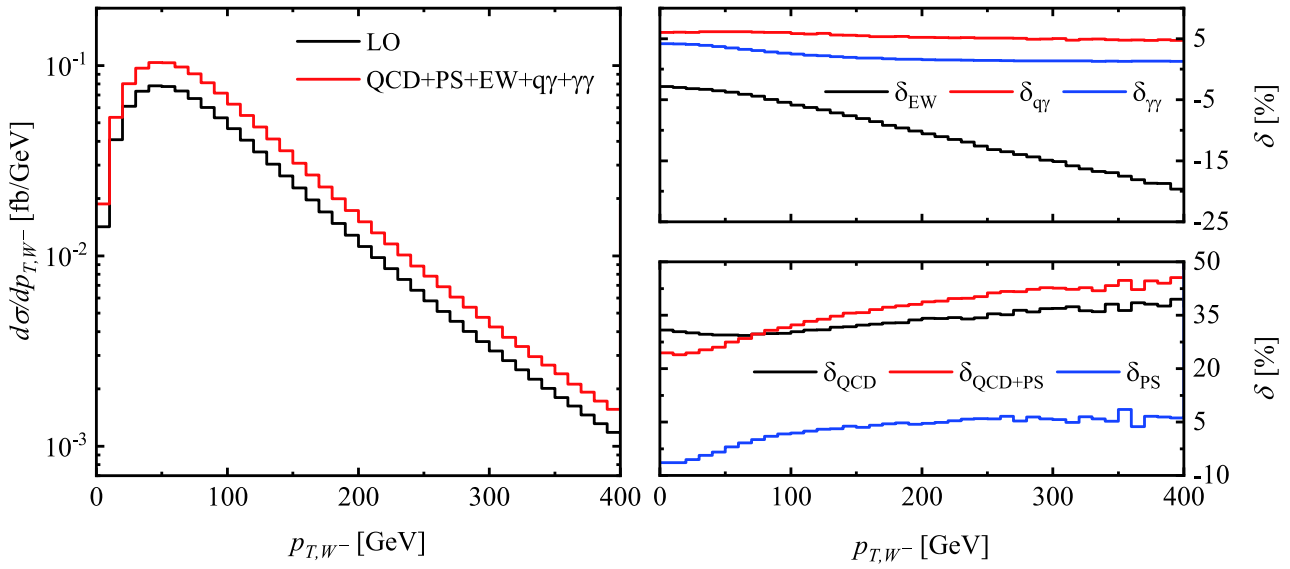

Fig. 6. (color online) The same as Fig. 5, but for transverse momentum distribution of W^-.

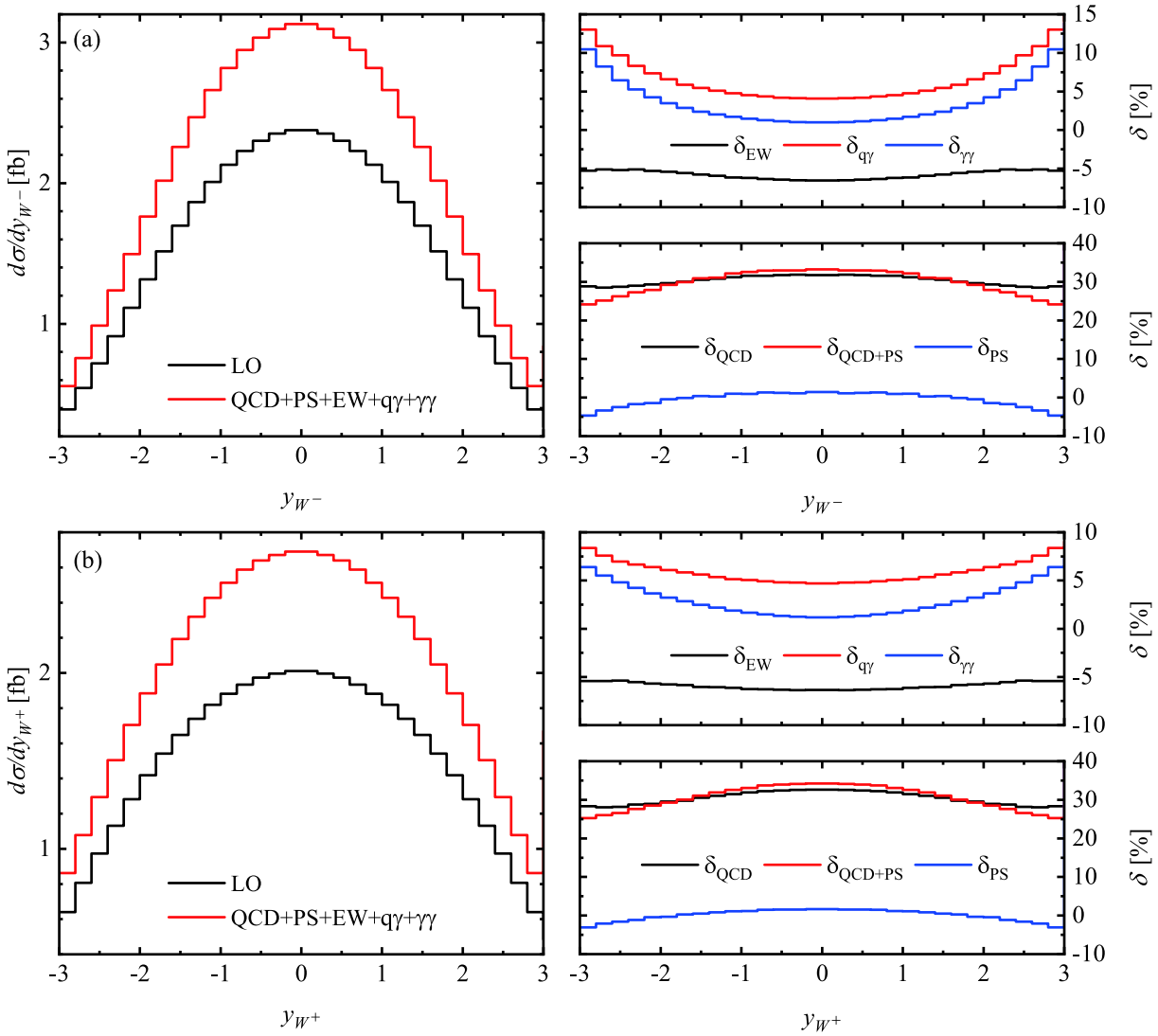

Fig. 7. (color online) As in Fig.5, but for rapidity distributions of W^- and W^+.

ive, and insensitive to the rapidities of W^- and W^+. It holds steady at about –5% in the entire plotted y_W region. The $q\gamma$-induced relative correction increases from about 5% to 13% and 8% for the rapidity distributions of W^- and W^+, respectively, with the increment of $|y_W|$ from 0 to 3. Compared to the $q\gamma$-induced relative correction, the $\gamma\gamma$-induced relative correction is relatively small. It is less than 10%, and increases slowly as the increment of $|y_W|$ for both W^- and W^+ rapidity distributions in the region of $|y_W| < 3$. The full photon-induced relative correction is sizeable, especially in the forward-backward rapidity region. We note the importance of the $q\gamma$ and $\gamma\gamma$ scattering channels and the cancelation between the photon-induced and $q\bar{q}$-initiated EW corrections in the W^- and W^+ rapidity distributions.

The Higgs-boson transverse momentum distributions and the corresponding strong and electroweak relative corrections are displayed in the left and right panels of Fig. 8, respectively. Both the LO and QCD + PS + EW + $q\gamma$+ $\gamma\gamma$ corrected Higgs transverse momentum distributions increase sharply in the low $p_{T,H}$ region ($p_{T,H} < 50$ GeV), reach their maxima at $p_{T,H} \sim 65$ GeV, and decrease approximately logarithmically when $p_{T,H} > 80$ GeV as the increment of $p_{T,H}$. The QCD+PS relative correction is positive, and increases from about 20% to 50% as $p_{T,H}$ increases from 0 GeV to 400 GeV. The $q\gamma$-induced relative correction is steady at about 3% in the low $p_{T,H}$ region and 10% in the region of $p_{T,H} > 250$ GeV, respectively, and increases smoothly in the intermediate $p_{T,H}$ region ($p_{T,H} \in [50, 250]$ GeV), while the $\gamma\gamma$-induced relative correction is 2% ~ 3% in the entire plotted $p_{T,H}$ region. The EW correction from the $q\bar{q}$ annihilation channel consistently suppresses the LO distribution, and the corresponding relative EW correction decreases from –2% to –18% as $p_{T,H}$ varies from 0 GeV to 400 GeV. In the high $p_{T,H}$ region, the $q\bar{q}$-initiated EW correction is sizable, and its absolute value is comparable to the QCD correction due to EW Sudakov logarithms.

The LO and QCD + PS + EW + $q\gamma$ + $\gamma\gamma$ corrected Higgs-boson rapidity distributions and the corresponding

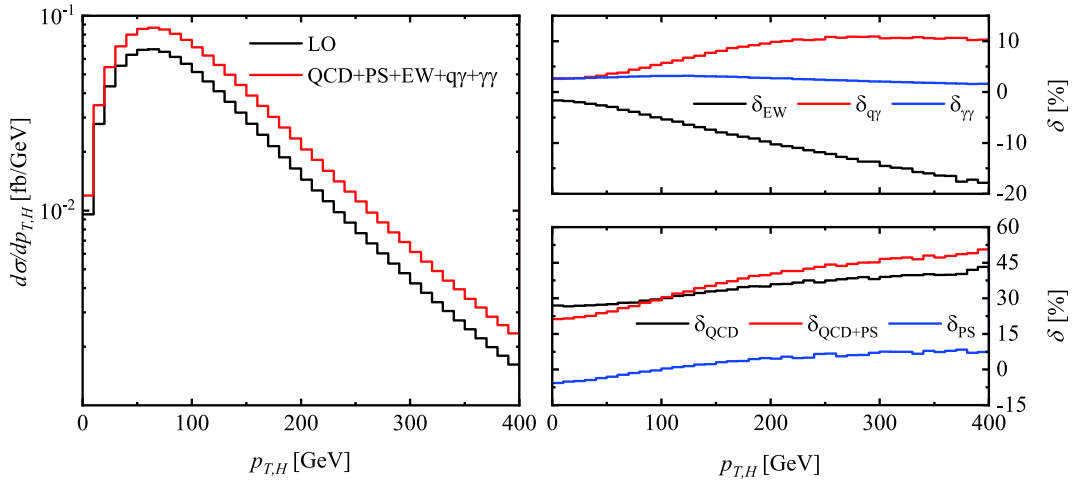

Fig. 8. (color online) As in Fig. 5, but for Higgs transverse momentum distribution.

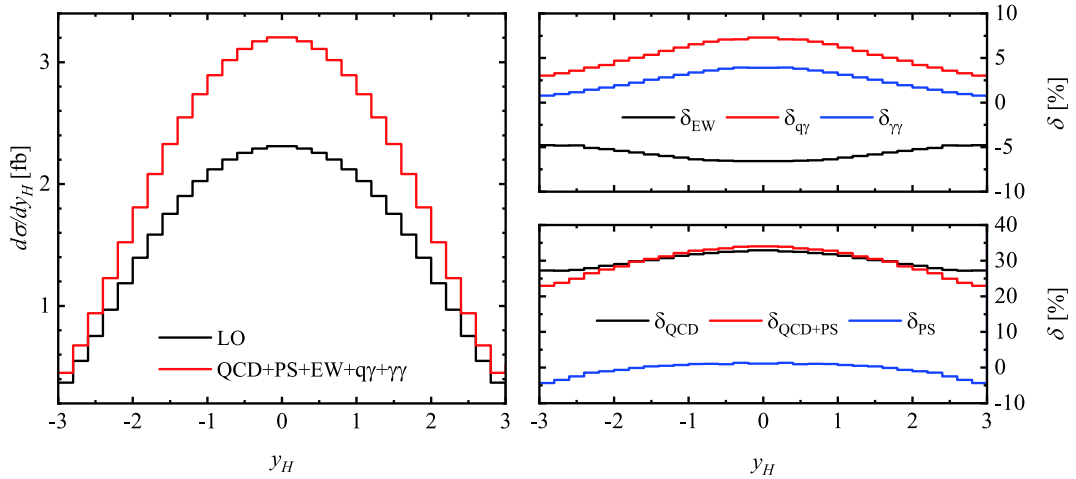

Fig. 9. (color online) As in Fig. 5, but for Higgs rapidity distribution.

relative corrections are shown in Fig. 9. Analogous to the W^- and W^+ rapidity distributions, the QCD+PS relative correction to the Higgs rapidity distribution decreases from 35% to about 25% as $|y_H|$ increases from 0 to 3, and the EW relative correction from the $q\bar{q}$ annihilation channel is insensitive to the Higgs rapidity and varies in the vicinity of −5% when $y_H \in [-3, 3]$. Both $q\gamma$- and $\gamma\gamma$-induced relative corrections are less than 10% in the region of $|y_H| < 3$. However, it should be noted that the photon-induced relative corrections to the Higgs rapidity distribution behave quite differently from those to the $W^\pm$ rapidity distributions. They decrease slowly with the increment of $|y_H|$ in the plotted y_H range.

3.3.2 Distributions for $pp \to W^-W^+H+X \to l^+l^-\nu_l\bar{\nu}_l b\bar{b}+X$

We turn to the W^-W^+H production with subsequent $W^\pm \to l^\pm\overset{(-)}{\nu}_l$ and $H \to b\bar{b}$ decays at the 14 TeV LHC. The spin correlation and finite-width effects of the intermediate Higgs and $W^\pm$ bosons are taken into account by adopting the MADSPIN method.

In the left panel of Fig. 10, we present the LO and QCD + PS + EW + $q\gamma + \gamma\gamma$ corrected invariant mass distributions of the final charged lepton pair for $pp \to W^-W^+H + X \to l^+l^-\nu_l\bar{\nu}_l b\bar{b} + X$. The corresponding strong and electroweak relative corrections are plotted in the bottom-right and top-right panels, respectively. Since the charged leptons are the decay products of $W^\pm$ bosons, the charged lepton-pair invariant mass distribution inherits the feature of the W-boson pair invariant mass distribution. Both the LO and QCD + PS + EW + $q\gamma + \gamma\gamma$ corrected charged lepton-pair invariant mass distributions peak at $M_{l^-l^+} \sim 75$ GeV, and decease approximately logarithmically as the increment of $M_{l^-l^+}$ in the range of $M_{l^-l^+} > 90$ GeV. In the low $M_{l^-l^+}$ region, the QCD + PS + EW + $q\gamma + \gamma\gamma$ correction is dominated by the QCD contribution, while in the high $M_{l^-l^+}$ region, the LO charged lepton-pair invariant mass distribution is mainly enhanced by the photon-induced corrections. The relative corrections from the $q\gamma$ and $\gamma\gamma$ scattering channels, for example, can reach about 55% and 85%, respectively, at $M_{l^-l^+} = 900$ GeV, while the QCD+PS relative correction is about 30% in the entire plotted $M_{l^-l^+}$ region. Thus, the photon-induced channels are not negligible for the precision measurement of $pp \to W^-W^+H + X \to l^+l^-\nu_l\bar{\nu}_l b\bar{b} + X$ at the 14 TeV LHC and future high-energy hadron colliders, especially for large $M_{l^-l^+}$.

Since the transverse momentum distribution of l^+ is similar to that of l^-, we only depict the transverse momentum distributions of l^- and the corresponding relative corrections in Fig. 11. Both the LO and QCD + PS + EW + $q\gamma + \gamma\gamma$ corrected p_{T,l^-} distributions reach their maxima at $p_{T,l^-} \sim 35$ GeV and then drop down as the increment of p_{T,l^-}. The QCD relative correction holds steady at about 30% in the low p_{T,l^-} region ($p_{T,l^-} < 50$ GeV) and subsequently increases to about 50% as p_{T,l^-} increases to 400 GeV. Because of the negative PS correction in the vicinity of $p_{T,l^-} \sim 35$ GeV, the QCD+PS relative correction decreases first, reaches its minimum at $p_{T,l^-} \sim 35$ GeV, and then gradually increases to about 60% as p_{T,l^-} increases to 400 GeV. The EW relative correction from the $q\bar{q}$ annihilation channel decreases consistently as the increment of p_{T,l^-} in the region of $p_{T,l^-} > 50$ GeV and reaches about −25% at $p_{T,l^-} = 400$ GeV due to the large EW Sudakov effect. The photon-induced relative corrections are insensitive to the transverse momentum of l^-: the $q\gamma$-initiated relative correction holds steady at about 6%, and the $\gamma\gamma$-initiated relative correction is about 2% ~ 4% in the entire plotted p_{T,l^-} region.

The LO, QCD + PS + EW + $q\gamma + \gamma\gamma$ corrected missing transverse momentum distributions and the corresponding relative corrections for $pp \to W^-W^+H + X \to$

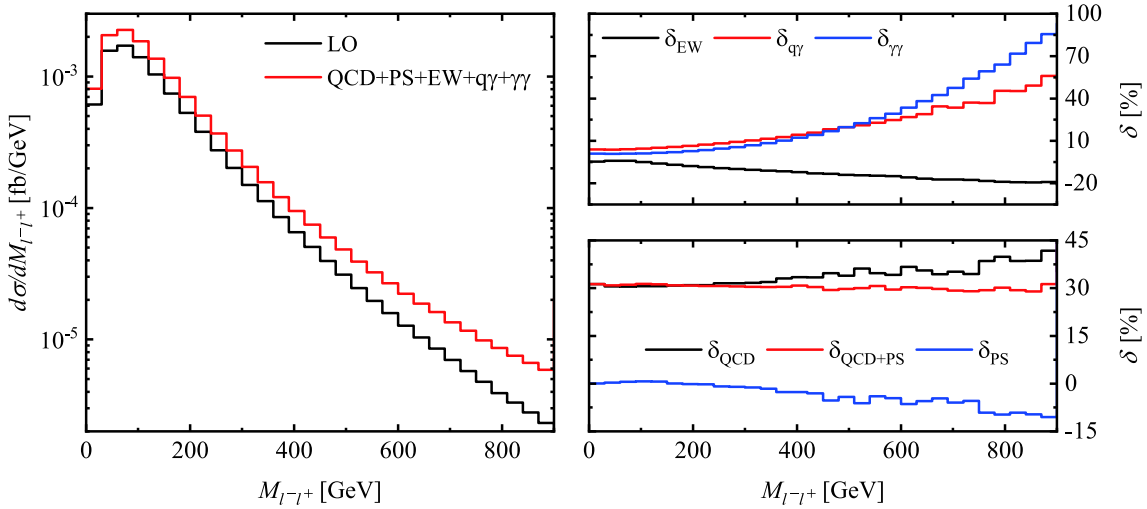

Fig. 10. (color online) Invariant mass distributions of charged lepton pair and corresponding relative corrections for $pp \to W^-W^+H \to l^+l^-\nu_l\bar{\nu}_l b\bar{b} + X$ at the 14 TeV LHC.

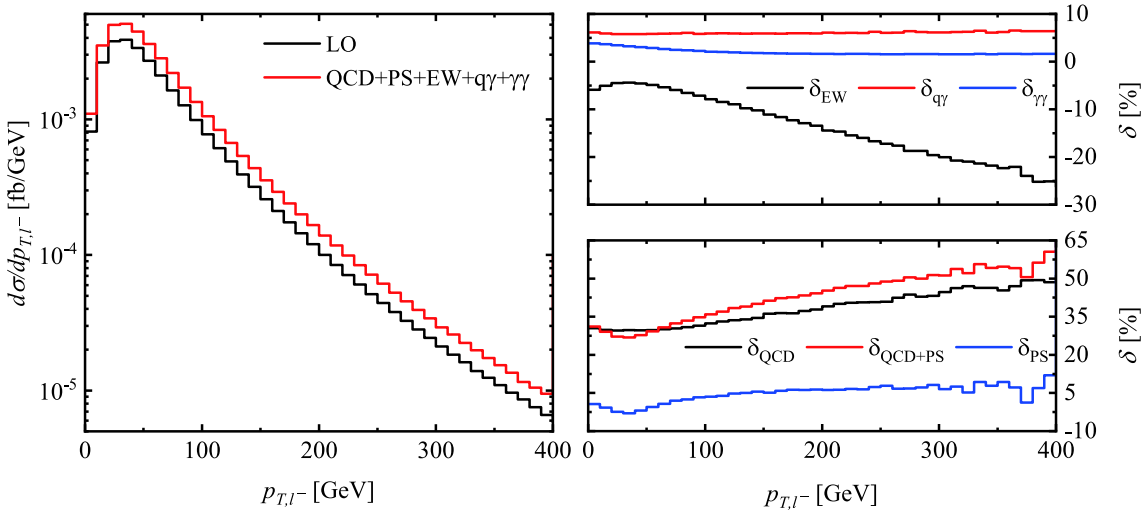

Fig. 11. (color online) As in Fig. 10, but for transverse momentum distribution of l^-.

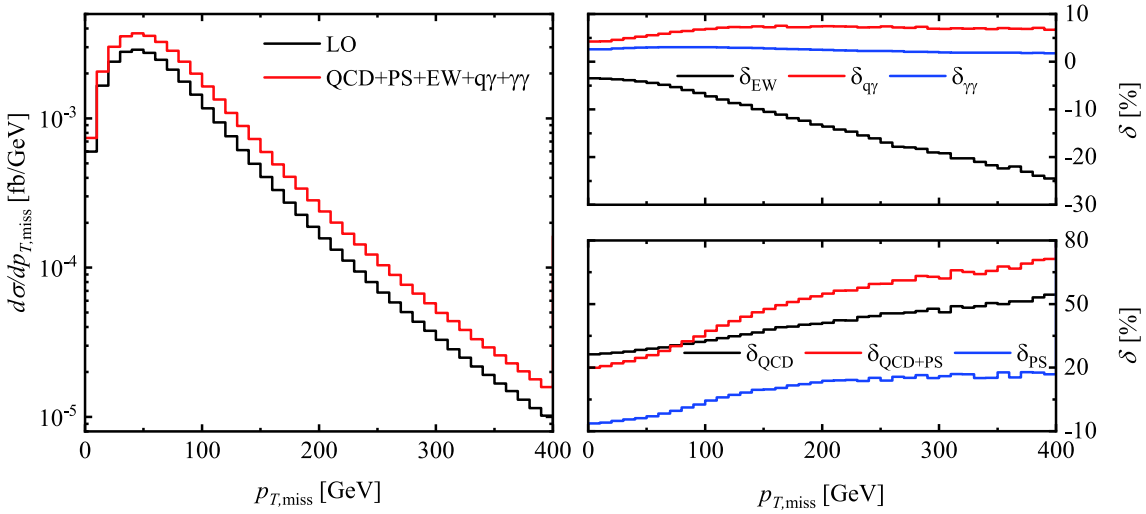

Fig. 12. (color online) The same as Fig.10, but for missing transverse momentum distribution.

$l^+l^-\nu_l\bar{\nu}_l b\bar{b}+X$ at the 14 TeV LHC are shown in Fig. 12. The corrections do not distort the line shape of the LO $p_{T,\mathrm{miss}}$ distribution, and both the LO and QCD + PS + EW+ $q\gamma+\gamma\gamma$ corrected $p_{T,\mathrm{miss}}$ distributions reach their maxima at $p_{T,\mathrm{miss}} \sim 45$ GeV. As the increment of $p_{T,\mathrm{miss}}$ from 0 GeV to 400 GeV, the QCD and QCD+PS relative corrections increase from 25% to 55% and from 20% to 70%, respectively, while the EW relative correction from the $q\bar{q}$ annihilation channel decreases from –3% to –25%. The relative corrections from the $q\gamma$ and $\gamma\gamma$ scattering channels are significant, but much less than the QCD+PS relative correction. They are almost independent of the missing transverse momentum, especially in the high $p_{T,\mathrm{miss}}$ region: the $q\gamma$-induced relative correction is about 7% and the $\gamma\gamma$-induced relative correction is 2% ~ 3%, respectively, as $p_{T,\mathrm{miss}} \in [100, 400]$ GeV.

The transverse momentum distribution of the final anti-bottom jet should be the same as that of the bottom jet due to the CP conservation in the $H \to b\bar{b}$ decay, such that we only study the b-jet transverse momentum distribution and discuss the influences of the QCD, PS, EW, $q\gamma$-induced, and $\gamma\gamma$-induced corrections on the $p_{T,b}$ distribution in the following. From Fig. 13, we see that both the LO and QCD + EW + $q\gamma+\gamma\gamma$ corrected b-jet transverse momentum distributions peak at $p_{T,b} \sim 45$ GeV, while the QCD + PS + EW + $q\gamma+\gamma\gamma$ corrected b-jet transverse momentum distribution reaches its maximum at $p_{T,b} \sim$ 65 GeV. Analogous to the p_{T,W^-}, $p_{T,H}$, p_{T,l^-}, and $p_{T,\mathrm{miss}}$ distributions, the b-jet transverse momentum distribution increases sharply in the low $p_{T,b}$ region and decreases approximately logarithmically after reaching its maximum as the increment of $p_{T,b}$. The QCD relative correction varies in the range of 30% ~ 45%, while the QCD+PS relative correction increases from approximately −90% to the

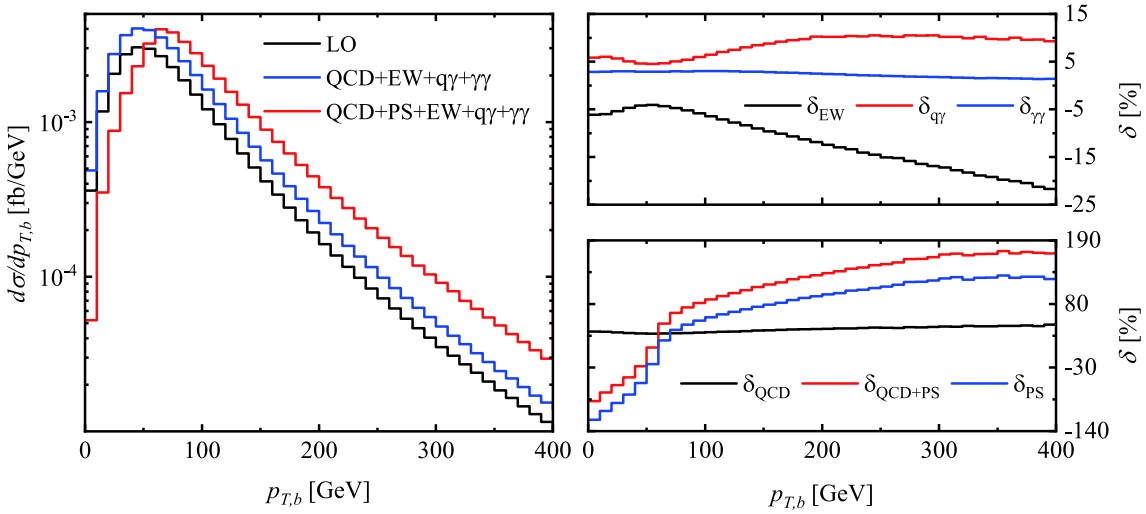

Fig. 13. (color online) As in Fig. 10, but for b-jet transverse momentum distribution.

order of 165%, as $p_{T,b}$ increases from 0 GeV to 400 GeV. This clearly shows that the PS correction to the b-jet transverse momentum distribution is more significant compared to the PS corrections to the kinematic distributions of colorless particles discussed above. Generally, the distributions of colored particles are more sensitive to PS effects than those of colorless particles, since the soft gluon can radiate from not only the initial-state partons, but also the final-state colored particles. Thus, the jet distribution is very sensitive to PS effects. The EW relative correction from the $q\bar{q}$ annihilation channel varies in the vicinity of –5% in the low $p_{T,b}$ region and then gradually decreases to approximately –20% as $p_{T,b}$ increases to 400 GeV. The $q\gamma$-induced relative correction ranges from about 5% to 10% for $p_{T,b} < 200$ GeV and holds steady at about 10% when $p_{T,b} > 200$ GeV. The $\gamma\gamma$-induced relative correction is insensitive to the b-jet transverse momentum. It is less than 3% and decreases very slowly as the increment of $p_{T,b}$ in the plotted $p_{T,b}$ region.

4 Summary

The production of W^-W^+H at the LHC can help to understand the EW symmetry breaking and search for new physics beyond the SM. In this study, we calculate the shower-matched NLO QCD correction and the $q\bar{q}$-, $q\gamma$-, and $\gamma\gamma$-initiated EW corrections to the W^-W^+H+X production at the 14 TeV LHC. We employ four different subtraction schemes to subtract the top-resonance effect for comparison, and we adopt the MADSPIN method to deal with the subsequent $W^\pm \to l^\pm \overset{(-)}{\nu}_l$ and $H \to b\bar{b}$ decays to preserve the spin correlation and finite-width effects as far as possible. The integrated cross section and some kinematic distributions of $W^\pm$ and H and their decay products are provided. The scale and PDF uncertainties of the integrated cross section are also given to estimate the theoretical error. Our numerical results show that the theoretical error of the $\mathrm{QCD}+\mathrm{EW}+q\gamma+\gamma\gamma$ corrected integrated cross section mainly originates from the renormalization scale dependence of the QCD correction. The QCD correction significantly enhances the LO differential cross section, especially in the central rapidity and high-energy regions, while the EW correction from the $q\bar{q}$ annihilation channel obviously suppresses the LO differential cross section. The QCD and $q\bar{q}$-initiated EW relative corrections to the integrated cross section are about 31% and –6%, respectively. The relative corrections from the photon-induced channels, $q\gamma \to W^-W^+Hq$, and $\gamma\gamma \to W^-W^+H$ are insensitive to the transverse momenta of final products. The $q\gamma$- and $\gamma\gamma$-induced relative corrections to the integrated cross section are about 6% and 3%, respectively, and they can compensate the negative EW relative correction from the $q\bar{q}$ annihilation channel. The PS relative corrections to the kinematic distributions of colorless particles are $O(10\%)$ in the bulk of the phase space, while the PS relative correction to the b-jet transverse momentum distribution can exceed 100% in the high $p_{T,b}$ region. Thus, we should take into account the shower-matched NLO QCD correction and EW corrections from the $q\bar{q}$ annihilation and photon-induced channels in precision study of the W^-W^+H production at the LHC and future hadron colliders.

References

1 S. L. Glashow, Nucl. Phys., **22**: 579 (1961)
2 S. Weinberg, Phys. Rev. Lett., **19**: 1264 (1967)
3 A. Salam, Conf. Proc. C, **680519**: 367 (1968)
4 P. W. Higgs, Phys. Rev. Lett., **13**: 508 (1964)
5 F. Englert and R. Brout, Phys. Rev. Lett., **13**: 321 (1964)
6 G. Aad et al (ATLAS Collaboration), Phys. Lett. B, **716**: 1 (2012)
7 S. Chatrchyan et al (CMS Collaboration), Phys. Lett. B, **716**: 30 (2012)
8 E. Gabrielli, M. Heikinheimo, L. Marzola et al, Phys. Rev. D, **89**: 053012 (2014)
9 C.-W. Chiang, X.-G. He, and G. Li, J. High Energy Phys., **08**: 126 (2018)
10 P. Agrawal, D. Saha, and A. Shivaji, arXiv: 1907.13168
11 CMS Collaboration (CMS Collaboration), CMS-PAS-FTR-15-002(2015)
12 CMS Collaboration (CMS Collaboration), CMS-PAS-HIG-16-024(2016)
13 A. M. Sirunyan et al (CMS Collaboration), Phys. Lett. B, **779**: 82 (2018)
14 J. Baglio, Phys. Rev. D, **93**: 054010 (2016)
15 J. Baglio, Phys. Lett. B, **764**: 54 (2017)
16 M. Song, W.-G. Ma, R.-Y. Zhang et al, Phys. Rev. D, **79**: 054016 (2009)
17 T. Hahn, Comput. Phys. Commun., **140**: 418 (2001)
18 D. T. Nhung, L. D. Ninh, and M. M. Weber, J. High Energy Phys., **12**: 096 (2013)
19 A. Sirlin, Phys. Rev. D, **22**: 971 (1980)
20 Y.-B. Shen, R.-Y. Zhang, W.-G. Ma et al, Phys. Rev. D, **95**: 073005 (2017)
21 A. Denner, S. Dittmaier, M. Hecht et al, J. High Energy Phys., **04**: 018 (2015)
22 A. Denner, S. Dittmaier, M. Hecht et al, J. High Energy Phys., **02**: 057 (2016)
23 J. R. Andersen et al, arXiv: 1405.1067
24 G. Passarino and M. Veltman, Nucl. Phys. B, **160**: 151 (1979)
25 Y. Zhang, W.-G. Ma, R.-Y. Zhang et al, Phys. Lett. B, **738**: 1 (2014)
26 A. Denner, Fortschr. Phys., **41**: 307 (1993)
27 B. W. Harris and J. F. Owens, Phys. Rev. D, **65**: 094032 (2002)
28 G. J. van Oldenborgh, Comput. Phys. Commun., **66**: 1 (1991)
29 A. Buckley, J. Ferrando, S. Lloyd et al, Eur. Phys. J. C, **75**: 132 (2015)
30 T. Hahn and M. Pérez-Victoria, Comput. Phys. Commun., **118**: 153 (1999)
31 P. Artoisenet, R. Frederix, O. Mattelaer et al, J. High Energy Phys., **03**: 015 (2013)
32 J. Alwall et al, J. High Energy Phys., **07**: 079 (2014)
33 T. Sjöstrand et al, Comput. Phys. Commun., **191**: 159 (2015)
34 E. Conte, B. Dumont, B. Fuks et al, Eur. Phys. J. C, **74**: 3103 (2014)
35 M. Cacciari, G. P. Salam, and G. Soyez, Eur. Phys. J. C, **72**: 1896 (2012)
36 R. Frederix, S. Frixione, V. Hirschi et al, J. High Energy Phys., **07**: 185 (2018)
37 L.-W. Chen, R.-Y. Zhang, W.-G. Ma et al, Phys. Rev. D, **90**: 054020 (2014)
38 R.-Y. Zhang, H. Yan, W.-G. Ma et al, Phys. Rev. D, **85**: 015017 (2012)
39 S. Frixione, E. Laenen, P. Motylinski et al, J. High Energy Phys., **07**: 029 (2008)
40 W. Hollik, J. M. Lindert, and D. Pagani, J. High Energy Phys., **03**: 139 (2013)
41 T. M. P. Tait, Phys. Rev. D, **61**: 034001 (1999)
42 A. S. Belyaev, E. E. Boos, and L. V. Dudko, Phys. Rev. D, **59**: 075001 (1999)
43 D. de Florian et al (LHC Higgs Cross Section Working Group), CERN Yellow Report No. CERN-2017-002-M (2017)
44 C. Patrignani et al (Particle Data Group), Chin. Phys. C, **40**: 100001 (2016)
45 A. Manohar, P. Nason, G. P. Salam et al, Phys. Rev. Lett., **117**: 242002 (2016)
46 B. Biedermann, A. Denner, and L. Hofer, J. High Energy Phys., **10**: 043 (2017)
47 A. Denner, J.-N. Lang, M. Pellen et al, J. High Energy Phys., **02**: 053 (2017)
48 G. Aad et al (ATLAS and CMS Collaborations), J. High Energy Phys., **08**: 045 (2016)
49 S. Alekhin et al, arXiv: 1101.0536